Small particle impact damage on different glass substrates

R. Waxman[a], I. Guven*[a] , P. Gray[b]
[a]Mechanical and Nuclear Engineering, Virginia Commonwealth University,
401 West Main Street, Richmond, VA 23284;
[b]Impact Testing Facility, Mail Stop EM41,
NASA/Marshall Space Flight Center, AL. 35812

ABSTRACT

Impact experiments using sand particles were performed on four distinct glass substrates. The sand particles were characterized using the X-Ray micro-CT technique; 3-D reconstruction of the particles was followed by further size and shape analyses. High-speed video footage from impact tests was used to calculate the incoming and rebound velocities of the individual sand impact events, as well as particle volume. Further, video analysis was used in conjunction with optical and scanning electron microscopy to relate the incoming velocity and shape of the particles to subsequent fractures, including both radial and lateral cracks. Analysis was performed using peridynamic simulations.

Keywords: Sand impact, fracture, radial crack, lateral crack, x-ray micro-CT, high-speed video, contact, peridynamics

1. INTRODUCTION

Window and dome material performance suffer from inadequate fracture resistance to sand particles and rain drops. Airborne sand particle impacts cause local damages that manifest themselves as radial, half-penny and lateral cracking, as shown in Figure 1. Erosion of surfaces through such impacts degrade optical properties of the materials. In order to mitigate impact damage due to small particles, an in-depth understanding of the origins of distinct fracture modes is necessary. While previously conducted work referenced in this paper involves theoretical approaches utilizing elasticity and plasticity formulations as well as experimental work [1–5], the dynamic nature of the impact is largely ignored. Furthermore, the impactors are chosen primarily because they have well understood geometry, such as Vickers indenters. Later work [6] used actual sand particles in the experiments as impactors. While it is valuable in understanding erosion resistance of different materials when impacted by specific size erodents, these studies did not explore direct relationships between impacting particles and subsequent damage modes.

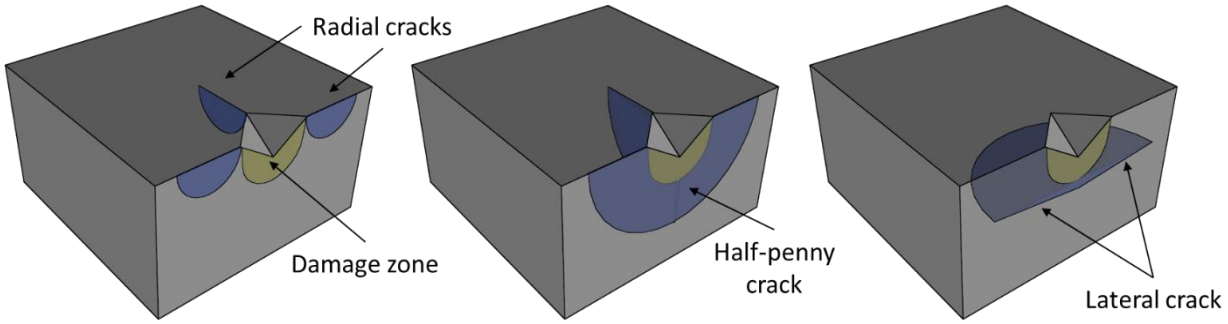

Figure 1. Description of radial, half-penny and lateral cracks.

This work presents the recent sand impact experiments performed on four distinct glass materials. A representative sampling of sand particles were characterized using X-Ray micro-CT technique and 3-D reconstruction of the particles were followed by further size and shape analyses. High-speed video footage was used to calculate the incoming and rebound velocities of the impact events. Further, video analysis was used in conjunction with microscopy, both optical and scanning electron, to relate the incoming velocity and shape of the particles to subsequent fractures, both radial and lateral. Additional analysis is presented utilizing peridynamic theory [7–12] for prediction of damage and fracture.

*iguven@vcu.edu; phone: 804-827-3652

2. EXPERIMENTAL SETUP

The experimental setup, shown in Figure 2, is located at NASA Marshall Space Flight Center. It uses compressed helium or argon to propel small particles. Two high-speed cameras are used to capture the impact event: Camera 1 (Side Cam) is placed on the side capturing the incoming and rebounding particles. Camera 2 (Top Cam) is situated on the opposite side of the barrel with the target material in between; the top camera is only useful when the target material is optically transparent. The focal plane of the top camera is coincident with the impacted surface allowing a good view of the sand particle at the time of the impact.

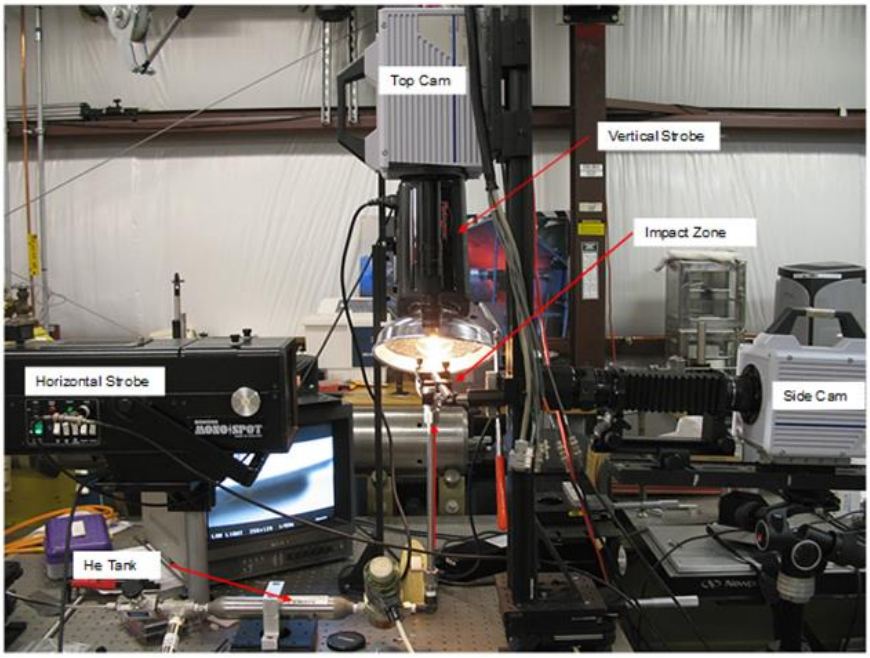

Figure 2. Experimental setup at NASA Marshall Space Flight Center.

3. SAND PARTICLE CHARACTERIZATION

The sand particles used in this study have size specification range of 149-177 um, which are characterized using x-ray CT-scan at Virginia Commonwealth University (VCU). Figure 3 (a) shows an x-ray image with sand particles clearly visible (red circles) along the vertical boundaries of the mid-section of the specimen holder. A black-and-white image from the top view is shown in Figure 3 (b) with sand particles visible (red circles) along the outer circular boundary. The x-ray images are then combined to reconstruct 3-D voxel representation of the sand particles as well as the specimen holder. Once the 3-D voxel reconstruction is complete, individual sand particles can be isolated for further examination.

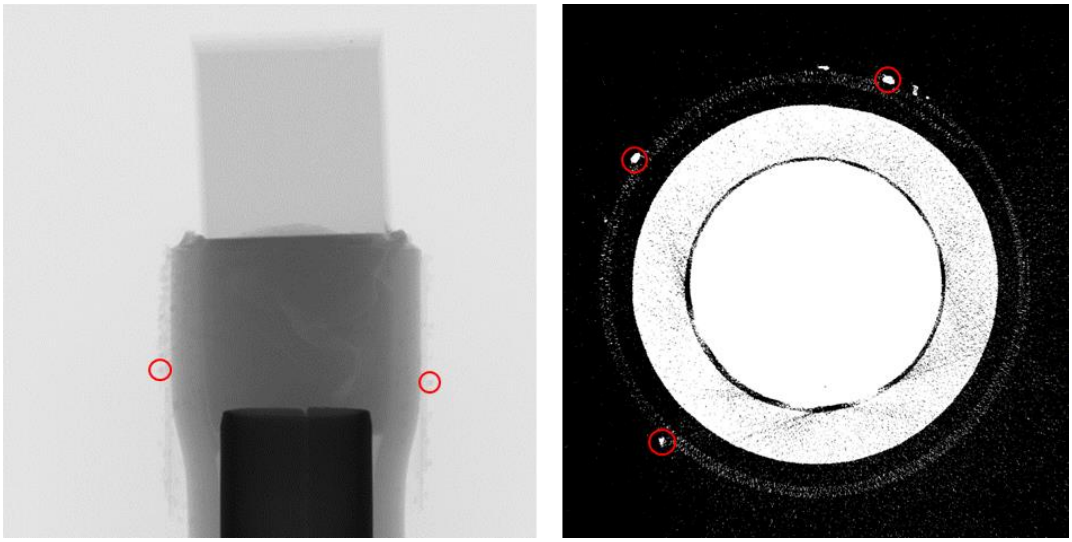

(a) (b)

Figure 3. X-ray CT-scan of cross-sections: (a) side view, and (b) top view.

Figure 4 illustrates a typical post-processing operation used to isolate and extract the voxel data for an individual sand particle; three orthogonal planes are shown with the sand particle of interest shown inside a bounding rectangular box. A number of still images are exported for each sand particle and processed using a custom in-house Python code to extract 3-D voxel coordinates. Figure 5 schematically demonstrates the 3-D reconstruction.

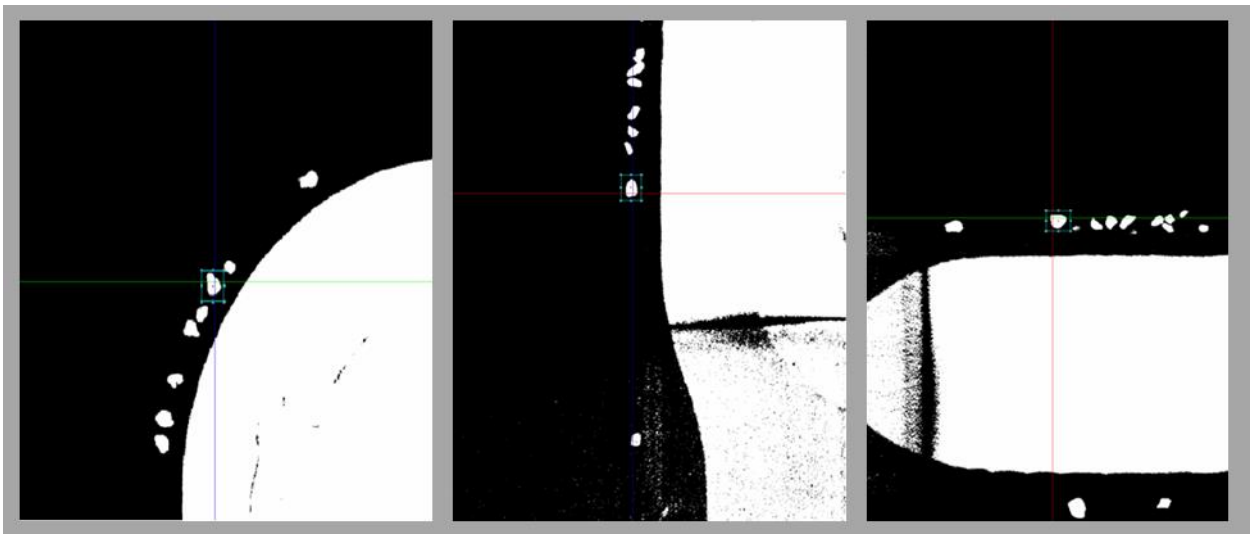

(a) (b) (c)

Figure 4. Cross-sectional views of a sand particle along three orthogonal planes.

Quantitative analysis of 53 sand particles is presented in the form of histograms in Figures 6 (a) through (c). The volume distribution shows the majority of the particles (45) are in the range of 1.0E6 to 1.2E7 um^3, with an average of 3.568E6 um^3. The surface areas of the particles are calculated based on a special algorithm implemented using Python that involves identifying the boundary voxels and counting their exposed surfaces. The histogram of the surface areas is shown in Figure 6 (b), ranging from 1.0E5 to 4.5E5 um^2, with an average of 2.011E5 um^2. Using the volume and surface area information, the "sphericity" Ψ of each particle was calculated using [13],

$$\Psi = \frac{\pi^3 (6V)^{\frac{2}{3}}}{A}, \tag{1}$$

in which V is the volume and A is the surface area of each sand particle. A sphere has a sphericity of unity. The histogram of sphericity (Figure 6 (c)) exhibits a large variation between 0.08 and 0.23, with an average 0.172, suggesting highly irregular shapes.

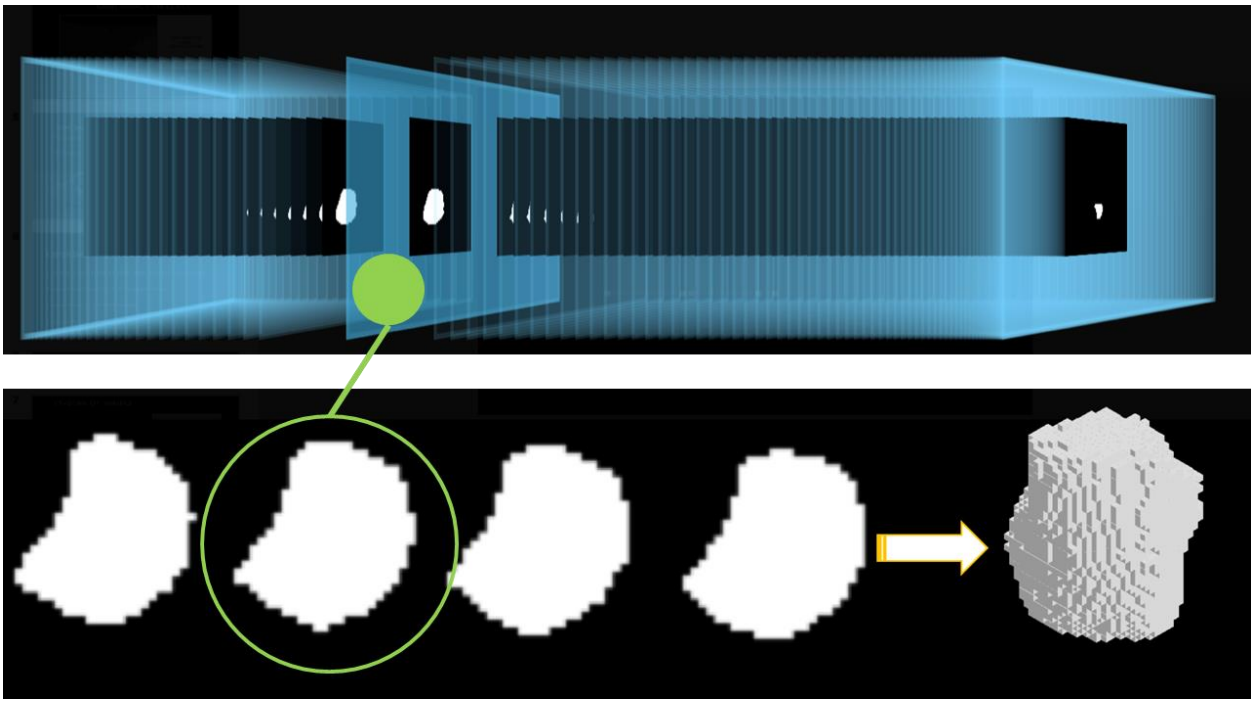

Figure 5. Schematic representation of 3-D reconstruction from a stack of images.

4. SAND IMPACT EXPERIMENTS

Four different target materials were selected for the sand impact experiments: (1) BK7, (2) Pyrex, (3) fused silica (FS), and (4) alumino-boro-silicate glass (ABS). The BK7, Pyrex, and FS samples were 1-inch-diameter disks that are 4 mm thick while the ABS glass is a 1-inch-square that is 1 mm thick. A total of 18 "shots" were performed on the four samples. Each shot involved multiple sand particles with a variety of incoming velocities. Figure 7 shows two typical sand impact sites examined using optical (left-most image) and SEM (3 images on the right). The two SEM images on the right in each row correspond to topography-mode, one producing "shadows" from left to right (labeled as Topo A) and the other producing shadows from top to bottom (labeled as Topo B). The topography mode is useful in understanding the relationship between the lateral and radial cracks as demonstrated in Figure 7 when the optical and SEM images are compared to each other. These images clearly show that the sub-surface lateral cracks propagate towards the surface and lift up enveloped by radial cracks. The optical and SEM images are used for measuring the radial and lateral cracks lengths presented later in this manuscript.

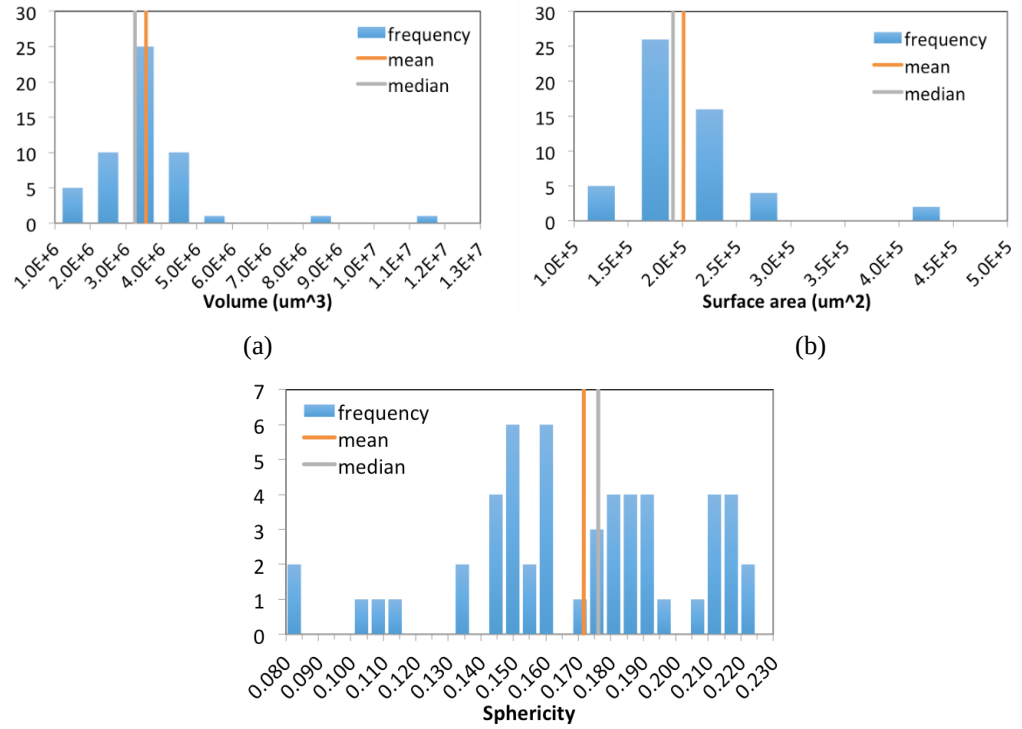

Figure 6. Quantitative examination of sand particles: Histograms of (a) particle volumes, (b) particle surface areas, and (c) particle sphericity, with mean and median shown.

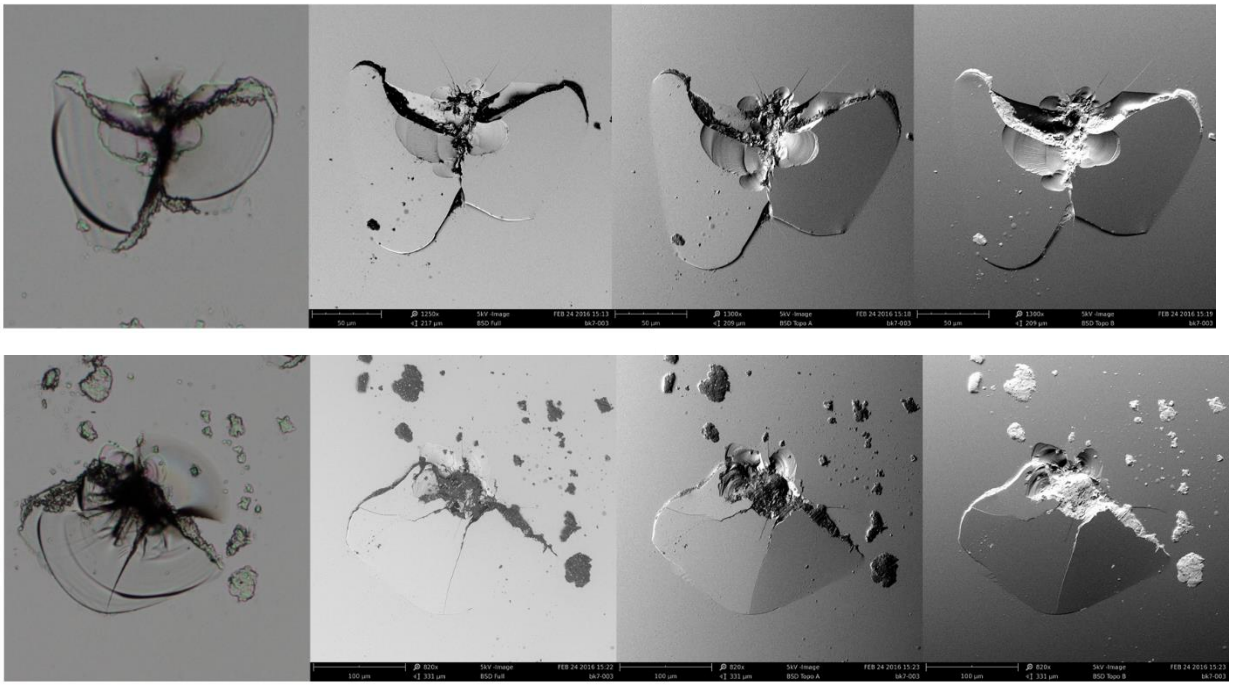

Figure 7. Optical and SEM images of two damage sites on the BK7 sample.

5. HIGH-SPEED VIDEO ANALYSIS

In order to explore the relationship between the micro-CT 3D reconstructed sand particles and those that were captured in the high-speed impact testing footage, each particle was matched with an impact location on the sample. Only particles that created damage that was recorded with the optical microscope were analyzed. The "after" image captured by the top camera was matched to the optical microscope images captured in-house. After valid impact sites were identified, the "after" image was overlaid on top of the high-speed footage during analysis in order to match particles with their respective impact sites.

The footage was viewed from the instant the particle appears on screen until it leaves frame, in order to ensure that no other particle or debris interfered with the flight path (see Figure 8). The travel distance of the particles was measured over a certain number of frames along with the time increment, which enables calculation of incoming and rebound velocities.

Figure 8. Flight path of a sand particle from the side camera.

From the video footage of impact testing, the volume of each sand particle was estimated. For each impact case, 3 to 6 frames were identified with a clear 2D image of the sand particle followed by drawing a rectangle encompassing the entire particle (see Figure 8), and calculating the area of each rectangle. The volumes of the imaginary rectangular boxes are calculated by an averaging the x and y extents and using the result as the third dimension. The volumes from all frames were then averaged to obtain a single volume estimate for each impact case. In order to infer actual particle volume based on the approximate rectangular prism volume from the video footage, the same calculations were performed on voxel data for 49 virtual sand particles obtained through x-ray micro-CT. It was found that the actual volume was approximately 0.356 times the estimated rectangular box volume, with a standard deviation of 0.109. Figure 9 presents the frequency distribution of the ratio of actual volumes to encompassing rectangular box volumes (i.e., scale factors). Based on these scale factors, the frequency distribution of the estimated particle volumes is shown in Figure 10. The video footage frame-by-frame images were also used to estimate the incoming and rebound velocities of the sand particles as shown in Figure 11.

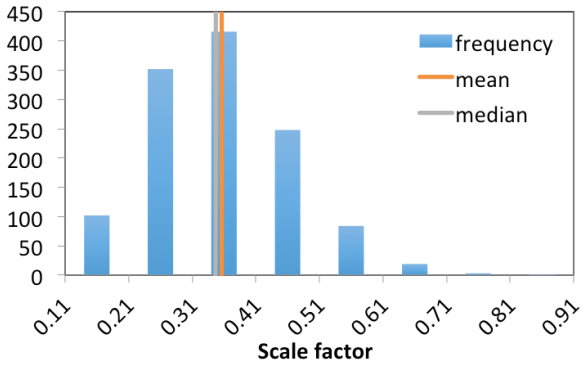

Figure 9. Frequency distribution of volume estimation scale factors, with mean and median shown.

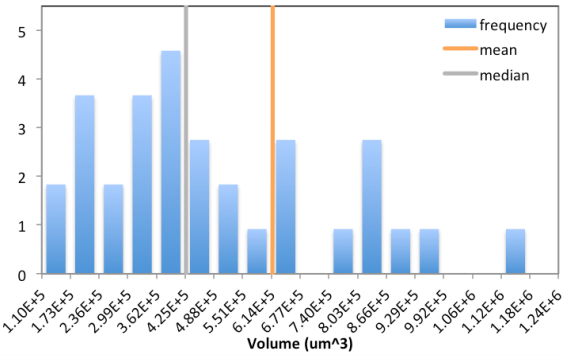

Figure 10. Frequency distribution of estimated particle volumes.

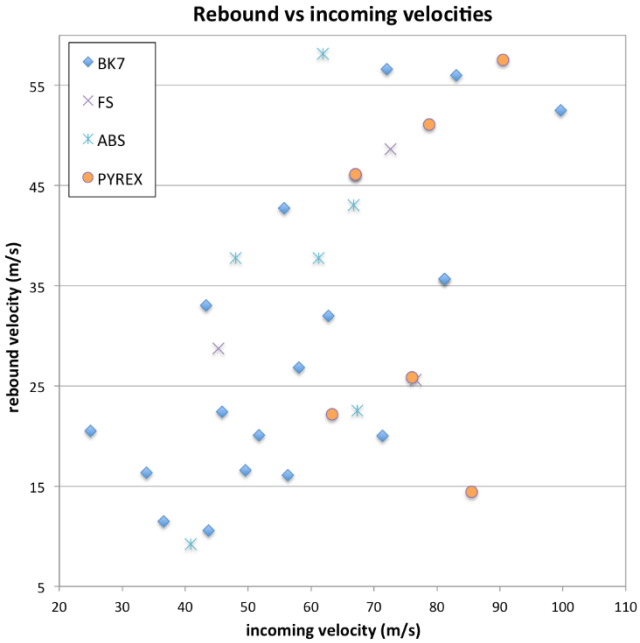

Figure 11. Incoming-rebound velocity pair distribution.

6. RESULTS

6.1 Quantitative Presentation of Fracture and Velocities

Analysis of a total of 31 impacts was performed, combining the observations from high-speed videos and evaluation of damage using microscopy. Damaged areas were separated into (a) contact damage areas and (b) lateral crack areas. A sample impact is shown in Figure 12. The three images are (a) optical microscopy, (b) SEM, and (c) SEM with damage outlines depicted. In Figure 12 (c), the red areas represent lateral cracks, labeled 1 and 2. The damage not in red represents the contact damage area. The impact event depicted involved a BK7 substrate, with an incoming velocity of 71.99 m/s and rebound velocity of 56.61 m/s. These measurements were performed for all 31 impact events. Figure 13 shows a summary of all impact events, separated by material. The yellow areas represent lateral cracks, while the red areas indicate contact damage areas. All damage areas are to scale across the figure. The green bars show incoming velocity, while the blue bars represent rebound velocity. All velocity bars are scaled across the figure as well, as indicated in the velocity bar scale in the bottom right. The black areas that can be seen to the right of four of the impact events (BK7 3-2 and 5-2, and Pyrex 8-1 and 11-1) represent the sand particle outlines seen in the high-speed video footage. These areas are to scale with each other, but not with the damage areas. Their scale bar can also be found in the bottom right, under additional scales.

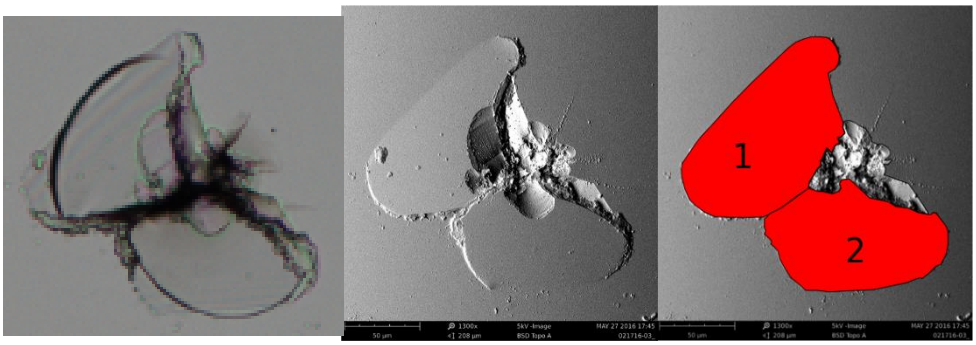

Figure 12. Sample damage outlines for BK7 sand impact: (a) optical microscopy, (b) SEM, (c) SEM with damage outlines depicted, lateral cracks in red, labeled 1 and 2.

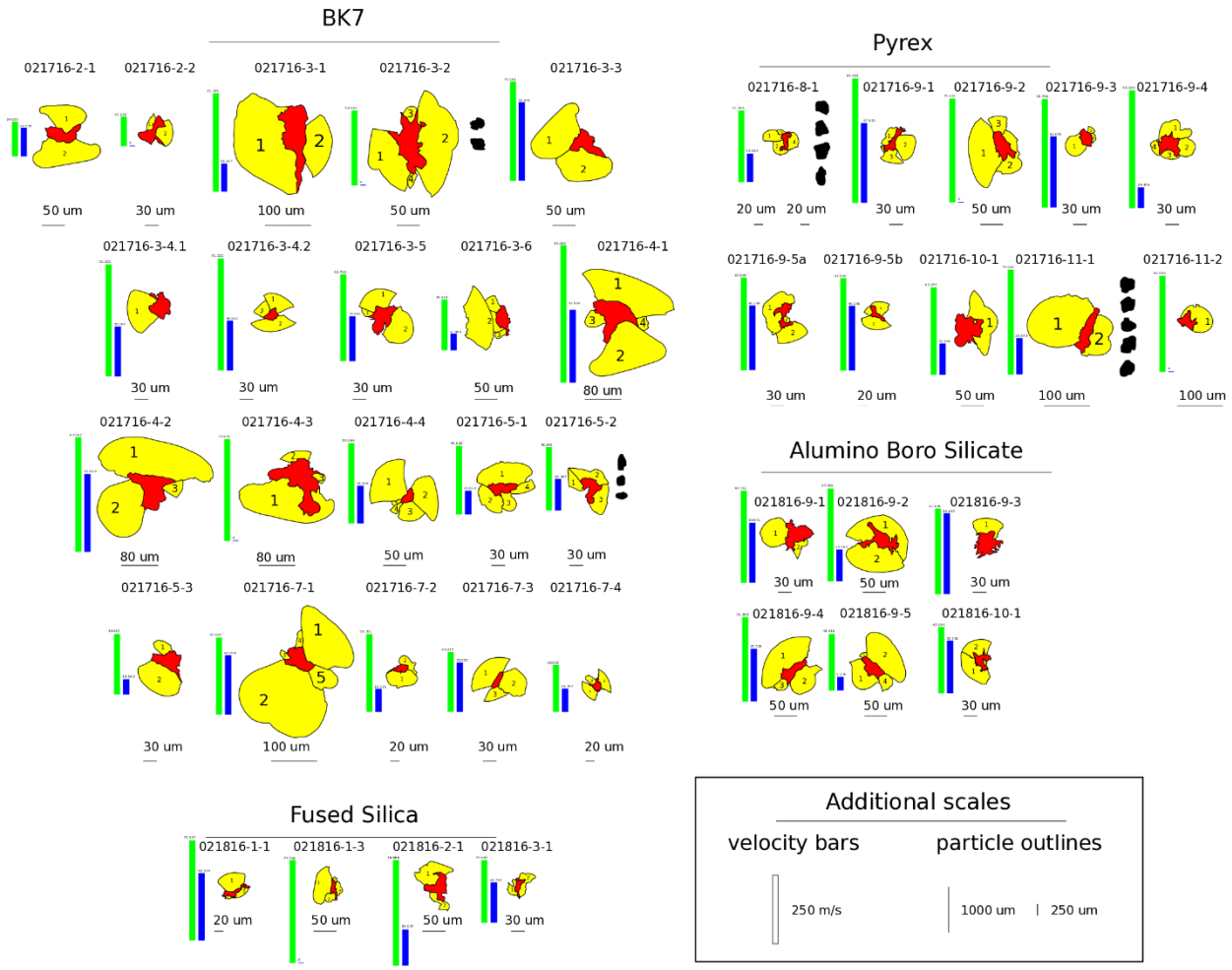

Figure 13. Summary of all impact event data: yellow areas show lateral crack damage, red areas show contact damage areas; green bars represent incoming velocity, blue bars indicate rebound velocity; black areas indicate sand particle shape and size in four impact events.

The purpose of the black areas is to show that within a substrate material, for similar particle sizes and incoming velocities, damage areas deviate vastly. This is a phenomenon that can be further seen in Figure 14, which shows damaged surface

area versus incoming kinetic energy, with a different marker for each substrate material. It can be seen that within a specific substrate material, for a similar kinetic energy value, a wide spread of damage occurred during different events.

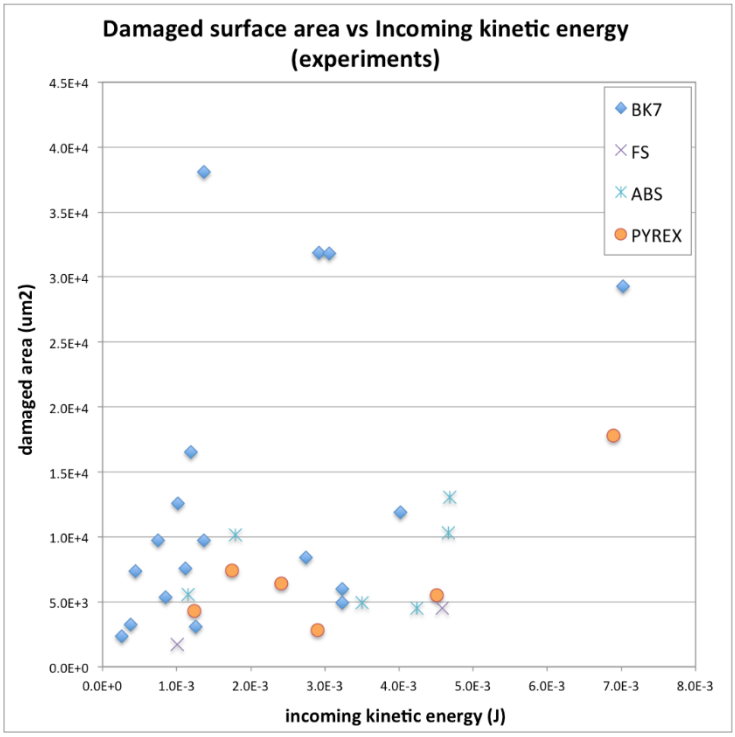

Figure 14. Damaged area versus incoming kinetic energy for sand impact events, separated by substrate material.

6.2 Peridynamic analysis (idealized cases here)

The large spread of damage caused by impact events with similar kinetic energy on the same substrate materials is clear in Figure 14. One possible contributor to this phenomenon is the variation in the impacting face geometries. A sand particle may have flat, round or sharp features depending on the approach angle. In order to explore the effects of impacting face geometries on the substrate damage, peridynamic simulations were performed with idealized geometries. Spheres and cylinder faces were used as extremes to demonstrate a rounded impact and flat impact, respectively. Material properties were assigned according to Table 1. where the sphere or cylinder impactor was treated as sand. The *sspnom* column refers to nominal speed of sound in each material; it is calculated based on material's bulk modulus and density. The *s*_crit and *v_inc* columns indicate critical stretch and incoming velocity values used, respectively. Tables 2 and 3 show the geometric properties of the cylinders and spheres used for impact. The lateral column indicates whether or not lateral cracks were present. The *r* column indicates radius, *h* indicates height, and *V* indicates volume. The *SA* value in the cylinder table is contact surface area. For all tests, cylindrical glass substrates had radius and height of 500um. In the cylinder cases, as diameter increased, height decreased. This was done in attempt to keep volume, and therefore kinetic energy, relatively consistent. Note that in the sphere cases this was not possible, as there is only one dimension to adjust. Therefore, as the sphere diameter increased, kinetic energy increased, as well.

Table 1. General information about peridynamic sand impact cases: *sspnom* refers to nominal speed of sound, *s_crit* indicates critical stretch value, *v_inc* is incoming velocity.

case	substrate material	density (g/mm^3)	sspnom (mm/s)	s_crit	v_inc (m/s)
021716-3.4	BK7	2.510E-3	3.6805E+6	0.0027	81.221
021816-1.1	FS	2.200E-3	4.0630E+6	0.0023	72.607
021816-9.2	ABS	2.400E-3	4.3519E+6	0.0031	67.376
021716-11.1	Pyrex	2.230E-3	4.0855E+6	0.0027	75.990
	sand	2.649E-3	4.1987E+6	0.03	

Table 2. Geometric properties of cylinder impactors.

cylinder	r (um)	h (um)	SA (um^2)	V (um^3)	lateral
cyl1	73.2	231.8	1.683E+4	3.9020E+6	no
cyl2	109.8	109.8	3.788E+4	4.1587E+6	no
cyl9	115.9	103.7	4.220E+4	4.3762E+6	no
cyl10	122	97.6	4.676E+4	4.5637E+6	no
cyl8	128.1	91.5	5.155E+4	4.7170E+6	yes
cyl7	152.5	67.1	7.306E+4	4.9024E+6	yes
cyl3	201.3	48.8	1.273E+5	6.2124E+6	yes

Table 3. Geometric properties of sphere impactors.

sphere	r (um)	V (um^3)	Lateral
sphere1	97.6	3.8944E+6	no
sphere2	122	7.6062E+6	no
sphere3	189.1	2.8325E+7	no

Peridynamic simulations were performed using deformable and rigid impactors. It was found that larger diameter impactors caused more damage to the substrate, for both cylinders and spheres. It was also found that larger cylinder impactors caused lateral cracks to appear beneath the substrate surface, while neither spheres nor smaller diameter cylinders caused such damage. An investigation was conducted to find that transition point for cylinders, where lateral cracks begin to form. With dimensions and materials properties previously outlined, that transition occurred at 128.1 um. Finally, it was shown that there was very little difference between the rigid, built-in penetrator and the deformable penetrator. Results are presented in Figures 15 through 17.

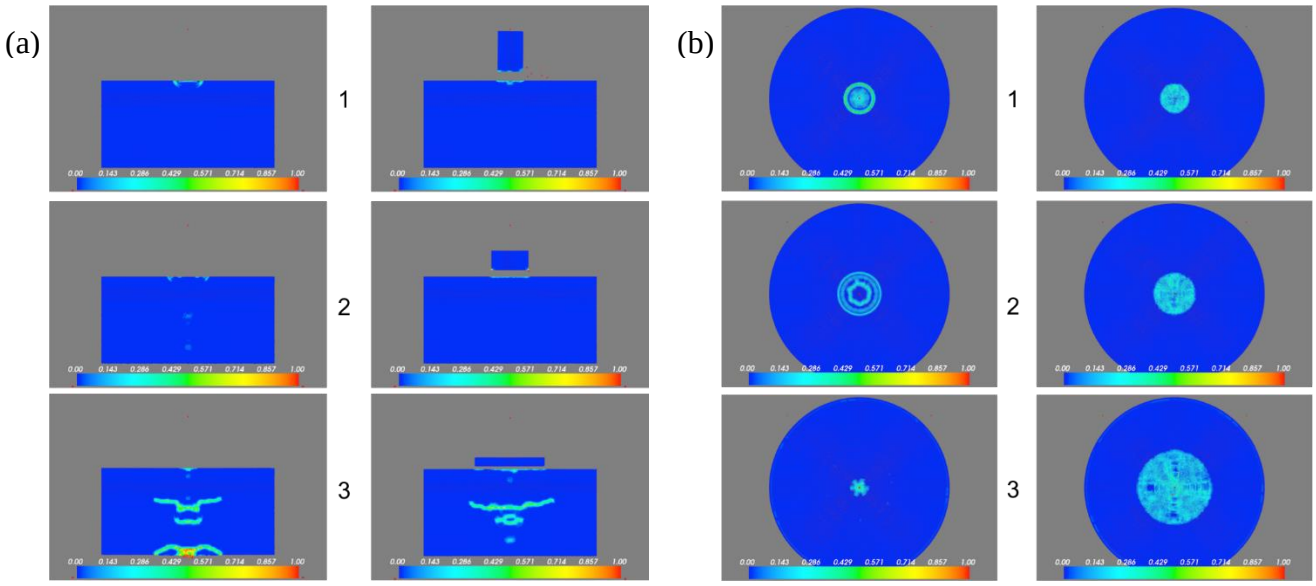

Figure 15. Cylinder damage results, built-in rigid penetrator, versus deformable penetrator: (a) section side view at center (x=0), and (b) top view of substrate

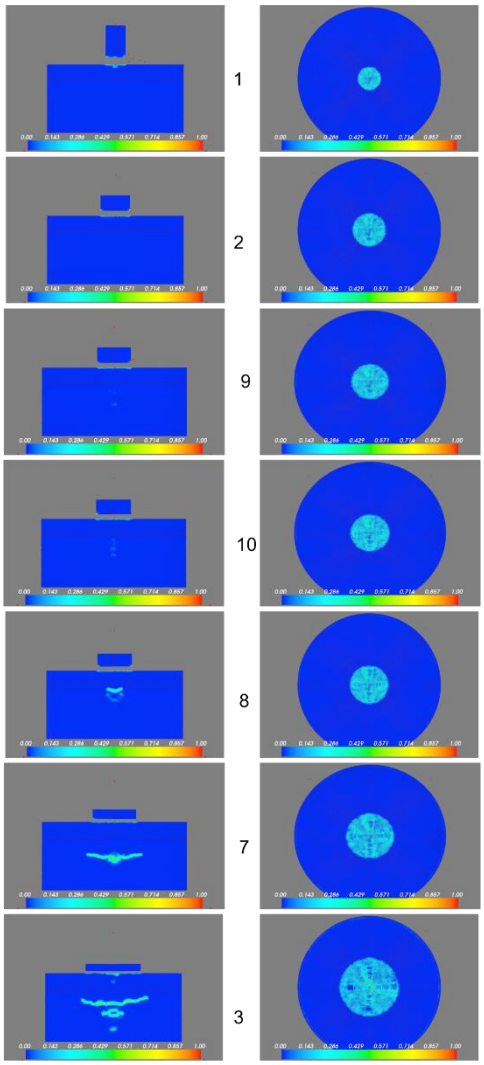

Figure 16. Cylinder damage results, deformable penetrator. Lateral cracks can be seen with cylinders 8, 7, and 3.

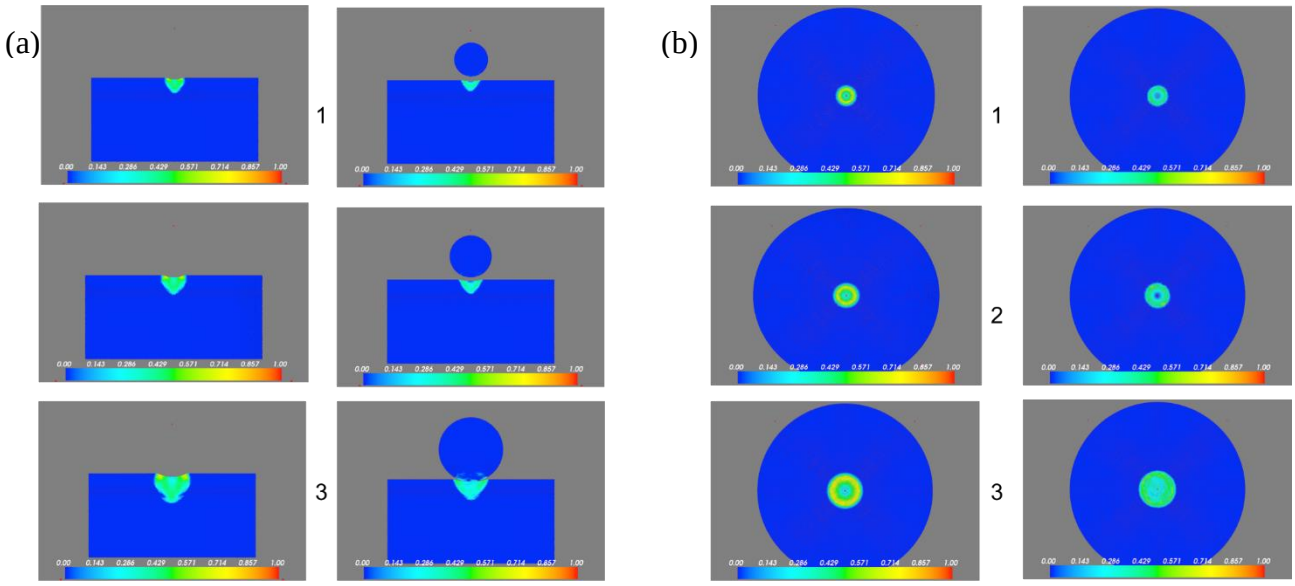

Figure 17. Sphere damage results, built-in rigid penetrator, versus deformable penetrator: (a) section side view at center (x=0), and (b) top view of substrate.

Further investigation was conducted to determine why, from the perspective of physics and measurable quantities, lateral cracks formed only for larger diameter cylinders, and not for smaller cylinders or any size sphere. Two possible explanations will be presented: impact duration and force on the penetrator. This calculation was performed for spheres 1 through 3 and cylinders 1 through 3, for both rigid and deformable impactors. A summary of impact duration data can be found in Figure 18. Results show that spheres have longer impact durations than cylinders for the same or similar diameters. Also, within spheres, as diameter increases, impact duration increases, while within cylinders, as diameter increases, impact duration decreases.

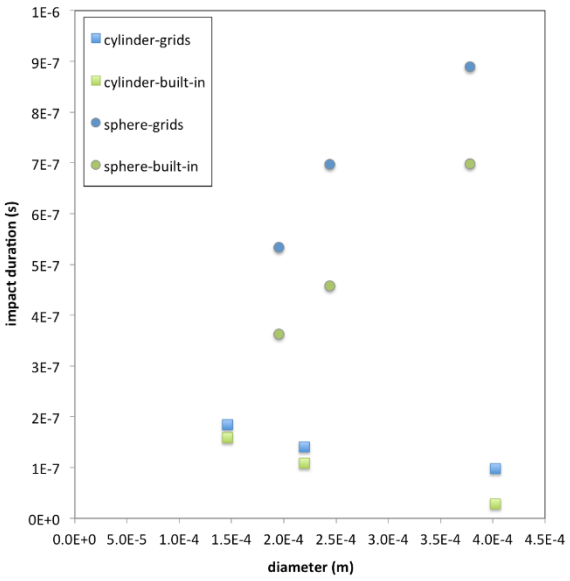

Figure 18. Impact duration versus diameter for cylinder and sphere impactors.

To calculate the normal component of force on the impactor, only the rigid penetrator cases were considered. Figures 19 (a) and (b) show this force plotted against diameter for cylinders and spheres, respectively. Figure 20 shows the maximum

normal force on the penetrator plotted against diameter, showing cylinders versus spheres. It can be seen that for the same diameter, cylinder impactors result in much higher normal force.

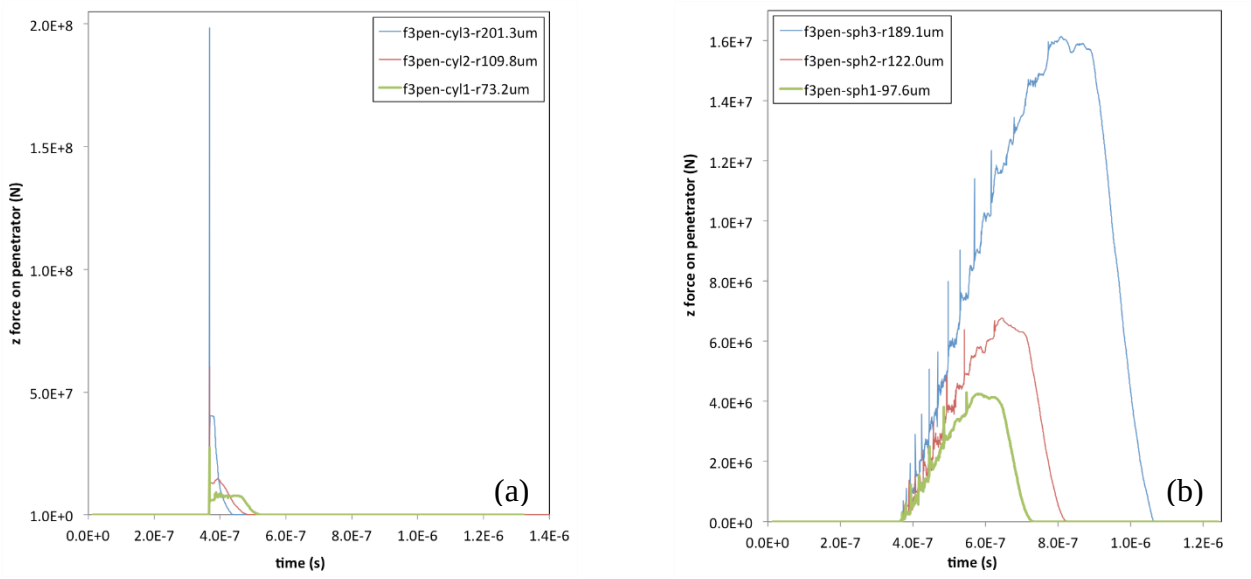

Figure 19. Normal component of force on penetrator for (a) cylinder impactors and (b) sphere impactors.

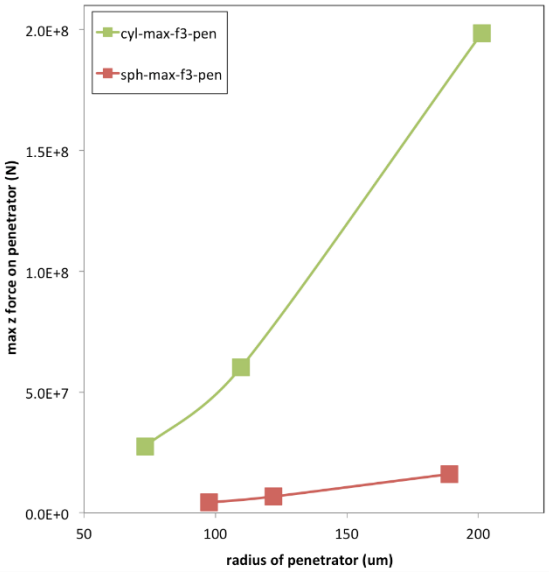

Figure 20. Maximum z-component of force on penetrator for cylinder and sphere impactors.

7. SUMMARY AND CONCLUSIONS

This study presented a number of sand impact experiments performed on four distinct glass substrates. An extensive characterization of sand particles using scanning electron microscopy and x-ray micro-CT technique has been presented, which led to 3-D reconstruction of the sand particles. This characterization effort allowed for detailed size and shape analyses of the sand particles used in the current study. During the tests, high-speed video recordings of each shot were

made from two orthogonal views. The high-speed videos permitted exploration of the relationship between the impacting particle shape and subsequent damage. Further analysis was performed to relate impacting geometries to the quantity and type of damage inflicted. The 3-D reconstructed sand particle geometries will be used in the follow-up simulation effort using peridynamic theory to further explore the underlying physics of the sand impact damage on brittle materials.

ACKNOWLEDGEMENTS

The authors would like to acknowledge Raytheon Company for providing the motivation for this study, and funding for earlier studies.

REFERENCES

[1] S. S. Chiang, D. B. Marshall, and a. G. Evans, J. Appl. Phys. **53**, 298 (1982).
[2] A. G. Evans and T. R. Wilshaw, Acta Metall. **24**, 939 (1976).
[3] D. B. Marshall, B. R. Lawn, and A. G. Evans, J. Am. Ceram. Soc. **65**, 561 (1982).
[4] B. R. Lawn and a. G. Evans, J. Mater. Sci. **12**, 2195 (1977).
[5] B. R. B. Lawn, A. G. Evans, and D. B. MARSHALL, J. Am. Ceram. Soc. **63**, 574 (1980).
[6] D. Harris, *Materials for Infrared Windows and Domes: Properties and Performance* (SPIE press, 1999).
[7] R. Schultz, I. Guven, and B. J. Zelinski, in *Proc. SPIE* (2015), p. 94530O.
[8] S. Tune, R. Schultz, I. Guven, and B. J. Zelinski, in *Proc. SPIE* (2015), p. 94530P.
[9] I. Guven and B. Zelinski, in *Proc. SPIE* (2015).
[10] S. A. Silling, J. Mech. Phys. Solids **48**, 175 (2000).
[11] S. A. Silling, M. A. Epton, O. Weckner, J. Xu, and E. Askari, *Peridynamic States and Constitutive Modeling* (2007).
[12] E. Madenci and E. Oterkus, *Peridynamic Theory and Its Applications* (Springer US, 2014).
[13] H. Wadell, J. Geol. **43**, 250 (1935).